

# Crystallization in a sheared colloidal suspension

Boris Lander,<sup>1</sup> Udo Seifert,<sup>1</sup> and Thomas Speck<sup>2</sup>

<sup>1</sup>*II. Institut für Theoretische Physik, Universität Stuttgart, Pfaffenwaldring 57, 70550 Stuttgart, Germany*

<sup>2</sup>*Institut für Theoretische Physik II, Heinrich-Heine-Universität Düsseldorf,  
Universitätsstraße 1, 40225 Düsseldorf, Germany*

We study numerically the crystallization process in a supersaturated suspension of repulsive colloidal particles driven by simple shear flow. The effect of the shear flow on crystallization is two-fold: while it suppresses the initial nucleation, once a large enough critical nucleus has formed its growth is enhanced by the shear flow. Combining both effects implies an optimal strain rate at which the overall crystallization rate has a maximum. To gain insight into the underlying mechanisms, we employ a discrete state model describing the transitions between the local structural configurations around single particles. We observe a time-scale separation between these transitions and the overall progress of the crystallization allowing for an effective Markovian description. By using this model, we demonstrate that the suppression of nucleation is due to the inhibition of a pre-structured liquid.

PACS numbers: 82.70.-y, 64.60.qe, 64.70.pv

## I. INTRODUCTION

The freezing of a disordered colloidal or nano suspension into a crystalline state with long-range order is a first-order phase transition that typically follows the nucleation and growth scenario [1]. While the stable crystalline phase is favored energetically, the interface with the disordered phase penalizes small nuclei and leads to a free energy barrier. Hence, for crystallization to commence, one has to wait for a rare fluctuation that results in a large enough *critical nucleus*, which subsequently grows until it spans the system. This implies that by avoiding nucleation the density of a suspension can be increased beyond the thermodynamic freezing density. Such a metastable state is called *supersaturated*. Simple expressions for the free energy barrier can be obtained within classical nucleation theory (CNT) [2–4], which assumes a spherical nucleus.

Subjecting a colloidal suspension to shear flow drives the system out of thermal equilibrium. Consequently, the concept of a free-energy is no longer well-defined and, strictly speaking, CNT cannot be applied anymore. Nevertheless, sheared colloidal suspensions still crystallize but with nucleation and growth kinetics that may be significantly altered from those in equilibrium [5, 6]. One might even find a dynamical coexistence of liquid and solid phases [7, 8]. Previous studies of the effects of shear flow on the crystallization rate are not conclusive: On one side, shear-enhanced crystallization has been reported for experiments [9–13] and numerical simulations [14, 15]. On the other side, a suppression of nucleation has been observed experimentally [16] and numerically [17, 18]. Others report an optimal strain rate for crystallization in supersaturated hard-sphere-like suspensions [19, 20] and protein solutions [21]. An optimal strain rate has also been reported in two dimensions for numerical simulations of Yukawa-type [22], Ising [23], and depletion-driven attractive [22] systems, and in a three-dimensional model glass [24].

Colloidal systems have the advantage that both the

spatial and temporal evolution can be monitored directly in experiments via light scattering [25–27], or in real space via confocal microscopy [20, 28], see also Ref. 29 for a review. Moreover, the interaction potential between colloidal particles can be tuned [30]. In the limit of perfect hard-spheres, the crystallization process is driven solely by entropy and the phase diagram depends on the density only. For repulsive interactions, temperature plays a role; the density is, however, still the dominant control parameter. For a numerical treatment, molecular dynamics as well as Brownian dynamics simulations appear to be ideally suited to track the temporal development of crystalline nuclei since particle coordinates are accessible and arbitrary interaction potentials can be used. However, since nucleation is hampered by a large free-energy barrier, it is a rare event. Depending on the height of the barrier, sampling such events can range from difficult to prohibitive unless specifically tailored methods are employed. Such methods include transition path sampling [31, 32], forward flux sampling [33, 34], and umbrella sampling [35, 36].

In this work, we present numerical results for a model colloidal suspension in three dimensions, where particles interact via hard-core exclusion plus a short-ranged Yukawa repulsion. The suspension is strongly supersaturated such that the probability for nucleation is shifted into a regime accessible by straightforward methods without making use of importance sampling schemes. Here, we employ underdamped Langevin dynamics. Although the suspension is strongly supersaturated, we observe that crystallization still proceeds via nucleation and growth. For the densities studied, small clusters appear and disappear until a cluster reaches the critical size. The following growth process is dominated by a single large cluster. We find that the time for this largest cluster to reach a specified size (larger than the critical size but smaller than the total number of particles) decreases for small strain rates but strongly increases at larger strain rates. There is, therefore, an optimal strain rate for the crystallization process. The reason is that shear flow is

responsible for two competing effects: suppression of the initial formation of a critical nucleus and enhancement of its growth once it has formed. Strain rates considered here are so low that shear-induced layering plays no role [9, 37].

For unsheared liquids it has recently been emphasized that nucleation resembles a two-stage process and that pre-structuring of the liquid plays a crucial role in the formation of the critical nucleus [38–41]: Droplets of the stable phase appear preferentially in regions of the supersaturated liquid that are still amorphous but where particles have already developed a loose connectivity with their neighbors. We confirm the two-stage scenario for the model studied here and demonstrate that the main effect of the shear flow is to disrupt the formation of such a pre-structured liquid. Hence, we find that the suppressed nucleation under shear flow has its origin in the inhibition of structuring in the liquid rather than in the “demolition” of crystalline clusters. The enhanced growth rate of sufficiently large clusters can be attributed to either convection or a faster reorganization of the cluster, making it thus easier to incorporate new particles.

The paper is organized as follows. In Sec. II, we present the system and simulation details. Moreover, we describe the structural order parameters that we employ to determine the structure of the local environment of single particles. In Sec. III, we present and discuss our simulation results for both the nucleation and growth stage before we conclude in Sec. IV.

## II. METHODS

### A. System and simulation details

We consider a mono-disperse colloidal suspension consisting of  $N = 4860$  particles in a simulation box of constant volume  $V$  with volume fraction  $\phi \equiv \pi N / (6V)$ . We study two densities with corresponding box dimensions  $17.709 \times 17.351 \times 18.404$  for  $\phi = 0.45$  and  $16.876 \times 16.535 \times 17.538$  for  $\phi = 0.52$ . Throughout the manuscript, we measure length in units of the particle diameter  $a$  and energy in units of the thermal energy  $k_B T$ , where  $T$  is the temperature of the suspension and  $k_B$  is Boltzmann’s constant. The time it takes for a particle to diffuse a distance corresponding to its diameter  $a$  defines the unit of time  $3\pi\eta a^3 / (k_B T)$ , where  $\eta$  is the viscosity of the solvent.

We employ underdamped Langevin dynamics given by  $\dot{\mathbf{r}}_k = \mathbf{v}_k$  and

$$m\dot{\mathbf{v}}_k = -\nabla_k U - [\mathbf{v}_k - \mathbf{u}(\mathbf{r}_k)] + \boldsymbol{\xi}_k, \quad (1)$$

with positions  $\mathbf{r}_k$  and velocities  $\mathbf{v}_k$ . We choose the dimensionless mass  $m = 1$  to be unity such that the relaxation time of the momenta equals the diffusive time-scale. The interaction forces are described by the potential

$$U = \sum_{i < j} u(|\mathbf{r}_i - \mathbf{r}_j|). \quad (2)$$

Thermal fluctuations are modeled by the stochastic forces  $\boldsymbol{\xi}$  with zero mean and correlations

$$\langle \boldsymbol{\xi}_i(t) \boldsymbol{\xi}_j^T(0) \rangle = 2\mathbb{1} \delta_{ij} \delta(t), \quad (3)$$

where  $\delta_{ij}$  denotes the Kronecker symbol,  $\delta(t)$  the Dirac distribution, and  $\mathbb{1}$  the identity matrix. Moreover, we impose an external linear shear flow by means of a solvent velocity field  $\mathbf{u}(\mathbf{r}) = \dot{\gamma} y \mathbf{e}_x$  entering the friction term, where  $\dot{\gamma}$  is the strain rate and  $\mathbf{e}_x$  the unit vector in  $x$  direction. In the simulations, we employ periodic boundary conditions using the Lees-Edwards sliding bricks method [42].

Particles interact pairwise via the repulsive Yukawa potential

$$u(r) = \begin{cases} \epsilon \frac{e^{-\kappa(r-1)}}{r} & (r \geq 1) \\ \infty & (r < 1) \end{cases} \quad (4)$$

with hard-core exclusion. The strength of the potential is given by the energy at contact  $\epsilon$ , and its range is determined by the inverse screening length  $\kappa$ . The magnitude of  $\kappa$  is mainly influenced by the ion concentration in the solvent and interpolates between Coulombic (low  $\kappa$ , low ion concentration) and hard-sphere interactions (large  $\kappa$ , high ion concentration). In this study, we choose  $\epsilon = 10$  and  $\kappa = 8$ . For this set of parameters, the freezing volume fraction is  $\phi^* \simeq 0.38$ . We are interested in the influence of a weak but steady shear flow on the crystallization dynamics of colloidal suspensions under highly supersaturated conditions ( $\phi = 0.45$  and  $0.52$ ).

The equations of motion (1) are integrated using a version of the velocity Verlet algorithm with time step  $\Delta t = 5 \times 10^{-4}$ . Initial configurations for different runs are generated by equilibrating the system at low densities ( $\phi = 0.2$ ). The volume fraction is then increased stepwise by rescaling the simulation box and the particle coordinates until the final volume fraction is reached. We use 20000 time steps. Once we reach the final volume fraction, we switch on the shear flow with strain rate  $\dot{\gamma}$ .

### B. Structure analysis

In order to describe the crystallization process quantitatively, we need a way to distinguish between liquid and solid structures. For the hard-core Yukawa system, the phase diagram of the equilibrium bulk structure includes, beside the liquid phase, the two crystalline structures body-centered cubic (bcc) and face-centered cubic (fcc) [1, 43, 44]. In the limit of hard-sphere interaction (high  $\kappa$ ), the free-energy difference between an fcc and a hexagonal close-packed (hcp) configuration is very low [45]. Therefore, hcp structures are likely to occur along with fcc structures, as has been observed in microgravity experiments [46]. For the parameters studied here, the bulk equilibrium structure is fcc. However, in the spirit of the Ostwald step rule [47], intermediate structures may be of a different type. Small nuclei,

e.g., have been found to belong predominantly to the bcc structure in a Lennard-Jones liquid [48]. Hence, in our analysis, we will not only discern fcc from the liquid state, but also include hcp and bcc-structures.

We employ different variants of the well-known Steinhardt order parameters [49] to determine the local environment of a single particle. The basic idea is to construct quantities sensitive to the rotational symmetry of the local environment of the particles. To that end, one locates the set of neighbors  $N_b(k)$  of the  $k$ th particle with size  $|N_b(k)|$  and computes the connecting vectors  $\mathbf{r}_{kj} \equiv \mathbf{r}_k - \mathbf{r}_j$  of the central particle with its  $j$ th neighbor, where a neighbor is defined as another particle within a range not exceeding  $R_b$ . This range is frequently chosen as the minimum between the first and second shell in the pair correlation function. We define the complex vector

$$q_{lm}(k) \equiv \frac{1}{|N_b(k)|} \sum_{j \in N_b(k)} Y_{lm}(\mathbf{r}_{kj}), \quad (5)$$

where the functions  $Y_{lm}$  are spherical harmonics and  $l > 0$ ,  $|m| \leq l$ . The vectors  $q_{lm}$  depend sensitively on the choice of  $l$ .

The first step is to distinguish fluid particles (disordered environment) from solid particles (ordered environment). To this end, we make use of a recently introduced variant of the Steinhardt order parameters that averages over the second-neighbor shell [50],

$$\bar{q}_l(k) \equiv \sqrt{\frac{4\pi}{2l+1} \sum_{m=-l}^l |\bar{q}_{lm}(k)|}, \quad (6)$$

where

$$\bar{q}_{lm}(k) \equiv \frac{1}{|N'_b(k)|} \sum_{j \in N'_b(k)} q_{lm}(j), \quad (7)$$

where  $N'_b(k)$  is the set of neighboring particles including the  $k$ th particle itself. Averaging the order parameter this way sharpens the distinction between different structures at the expense of spatial resolution. For  $l = 6$ , the probability distributions of  $\bar{q}_6$  for fluid and solid particles are well separated, providing a good way to discriminate these two basic structure types from each other (data not shown). We regard a particle as fluid if  $\bar{q}_6 < 0.4$  and as solid otherwise.

Having determined these two particle sets, we further split the fluid particles into two subsets: liquid and pre-structured. While liquid particles have a truly disordered environment, we identify particles as pre-structured that have an environment that does not qualify as solid but where nevertheless some “bonds” between particles have formed. To concretize the concept of a bond, we consider

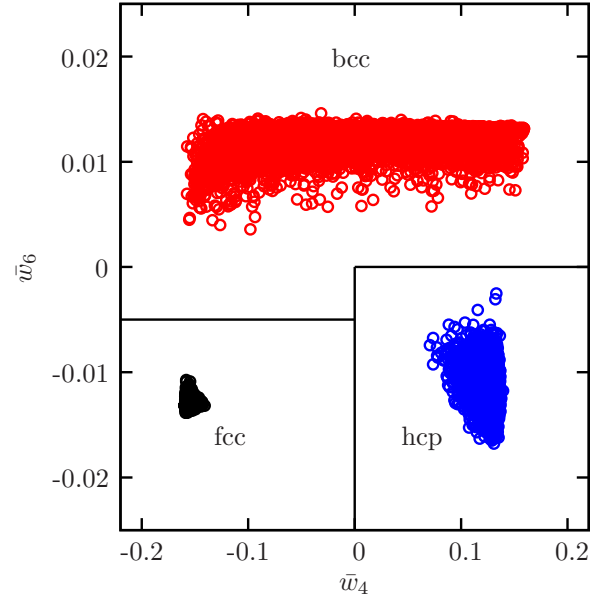


FIG. 1: Scatter plot of  $\bar{w}_4$ - $\bar{w}_6$  trajectories for perfect hcp, bcc, and fcc crystals subject to thermal fluctuations. The  $\bar{w}_4$ - $\bar{w}_6$  plane is divided into the indicated regions, which are used to determine the crystal structure of solid particles.

the normalized scalar product

$$S_{kj}^{(l)} \equiv \frac{\sum_{m=-l}^l q_{lm}(k) q_{lm}^*(j)}{\left( \sum_{m=-l}^l q_{lm}(k) q_{lm}^*(k) \right)^{1/2} \left( \sum_{m=-l}^l q_{lm}(j) q_{lm}^*(j) \right)^{1/2}}, \quad (8)$$

with  $q^*$  the complex conjugate of  $q$ . This product defines a measure for the strength of the correlation between the surrounding structures of the  $k$ th and the  $j$ th particle. We regard two neighboring particles as “bonded” if  $S_{kj}^{(6)} > 0.5$  [51] and denote the number of bonds for the  $k$ th particle as  $n_{\text{bonds}}$ . While also in the liquid particles will have bonds, we consider particles that have at least 8 bonds with neighboring particles (but still  $\bar{q}_6 < 0.4$ ) as pre-structured.

Finally, by employing another type of averaged order parameters [50]

$$\bar{w}_l(k) \equiv \frac{\sum_{m_1+m_2+m_3=0} \begin{pmatrix} l & l & l \\ m_1 & m_2 & m_3 \end{pmatrix} \bar{q}_{lm_1}(k) \bar{q}_{lm_2}(k) \bar{q}_{lm_3}(k)}{\left( \sum_{m=-l}^l |\bar{q}_{lm}(k)|^2 \right)^{3/2}}, \quad (9)$$

we are able to discern the different crystalline structures within the solid particles. The term in brackets is the Wigner-3-j symbol, which is related to Clebsch-Gordan coefficients. The sum runs over all combinations of  $m_1$ ,  $m_2$  and  $m_3$  with  $m_1 + m_2 + m_3 = 0$ . Using two parameters  $\bar{w}_4$  and  $\bar{w}_6$ , we obtain a good separation between

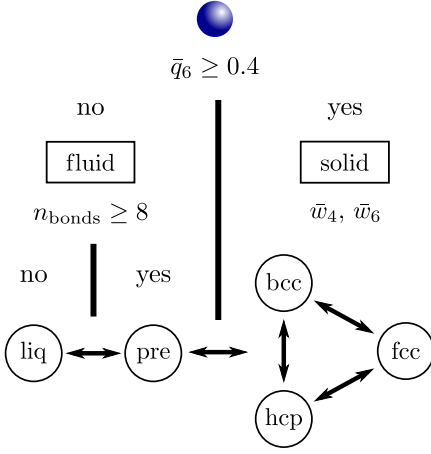


FIG. 2: Decision tree for the assignment of a structure to a particle. On the first level, the particle is classified either as fluid or solid. On the second level, the fluid particles are split into pre-structured and liquid particles, while the solid particles are subdivided into the crystalline structures hcp, bcc, and fcc. The double-headed arrows indicate the transitions we observe primarily during the crystallization process: While among the solid structures all transitions occur, the liquid particles almost never reach a crystalline state without passing through a pre-structured configuration first.

the distributions in the  $\bar{w}_4\bar{w}_6$  plane, see scatter plot in Fig. 1. The  $\bar{w}_4$  distribution is widely separated for hcp and fcc structures, while  $\bar{w}_6$  separates bcc from hcp and fcc. Hence, a solid particle is classified as fcc if  $\bar{w}_4 \leq 0$  and  $\bar{w}_6 \leq -0.005$  (lower left region), as hcp if  $\bar{w}_4 > 0$  and  $\bar{w}_6 \leq 0$  (lower right region), and as bcc otherwise (upper region). Fig. 2 illustrates the complete classification process. Moreover, it shows the possible transitions between the different structures occurring during the crystallization. Between the solid states, each of the transitions occurs. However, the transitions are biased towards an fcc environment. As we will see in the following, direct transitions from the liquid into a crystalline state are rare and the solidification of a liquid particle generally advances through a pre-structured state first.

### C. Discrete state model

The structure analysis enables us to categorize single particles according to their local environment. For a given configuration of particle positions at time  $t$ , we define an indicator function  $h_k(t)$  for every particle  $k$  which takes on one of the five values: liquid (liq), pre-structured (pre), hcp, bcc, or fcc. The population (fraction of particles) of structure type  $i$  is

$$c_i(t) \equiv \frac{1}{N} \sum_{k=1}^N \delta_{i,h_k(t)}. \quad (10)$$

As the suspension evolves, the structural environment of particles will of course change. To quantify these changes

we define the fluxes

$$f_{i \rightarrow j}(t) \equiv \sum_{k=1}^N \delta_{i,h_k(t)} \delta_{j,h_k(t+\delta t)}, \quad (11)$$

which count the number of particles that have been converted from structure  $i$  into structure  $j$  within the time interval  $[t, t + \delta t]$ . If not indicated otherwise, we set  $\delta t = 100\Delta t$ .

In the following, we consider the size  $n$  of the largest cluster as an order parameter characterizing the progress of the crystallization process. Clusters are identified as the sets of all solid particles that are mutually bonded (in the sense defined above that  $S_{kj}^{(6)} > 0.5$ ). We define the average population at fixed cluster size  $n$  in the suspension as the conditional average

$$\bar{c}_i(n) \equiv \langle c_i(t) \delta_{n,n(t)} \rangle / Z_n, \quad (12)$$

where  $\langle \cdot \rangle$  averages over time and over different realizations of the crystallization process. Hence,  $Z_n \equiv \langle \delta_{n,n(t)} \rangle$  counts how many times the largest cluster size  $n$  occurs in all runs considered. Moreover, we define a  $5 \times 5$  transfer matrix  $\mathbf{T}$ , the components of which are given by the fluxes as

$$T_{i \rightarrow j}(n) \equiv \left\langle \frac{f_{i \rightarrow j}(t)}{N c_i(t)} \delta_{n,n(t)} \right\rangle / Z_n \quad (13)$$

with normalization  $\sum_j T_{i \rightarrow j} = 1$ . The component  $T_{i \rightarrow j}(n)$  of this stochastic matrix quantifies the fraction of particles in state  $i$  that convert on average into state  $j$  within the time interval  $\delta t$ . The eigenvalues of  $\mathbf{T}$  can be sorted,  $\lambda_0 > \lambda_1 > \dots > \lambda_4$ , with  $\lambda_0 = 1$ . The components of the corresponding right-hand-side eigenvectors fulfill

$$\sum_i w_i^{(0)} = 1, \quad \sum_i w_i^{(\alpha)} = 0 \quad (\alpha \geq 1). \quad (14)$$

The product  $\mathbf{T}(n(t))\mathbf{c}(t) = \mathbf{c}(t + \delta t)$  yields the average population a time  $\delta t$  later with  $\mathbf{c}(t) \equiv (c_i(t))$ . Applying the transfer matrix repeatedly describes an effective Markovian dynamics *at fixed cluster size*. Under this dynamics, the average population after a time  $\tau$  has elapsed becomes

$$\mathbf{c}(\tau) = \mathbf{w}^{(0)} + \sum_{\alpha=1}^4 \zeta_\alpha \mathbf{w}^{(\alpha)} e^{-\tau/\tau_\alpha} \quad (15)$$

with implied time scales  $\tau_\alpha(n) \equiv -\delta t / \ln \lambda_\alpha(n)$  and coefficients  $\zeta_\alpha \equiv \mathbf{w}^{(\alpha)} \cdot \mathbf{c}(0)$ . Hence, for  $\tau \gg \tau_1$ , the system approaches a (quasi)-stationary average population given by  $\mathbf{w}^{(0)}$ . The relaxation time is determined by  $\tau_1$ .

For a freely evolving suspension, the size of the largest cluster is of course not constrained to a fixed  $n$ . Suppose there is a time-scale separation: After a change of  $n$  the system relaxes into the quasi-stationary state before the cluster size changes again. Then the actual

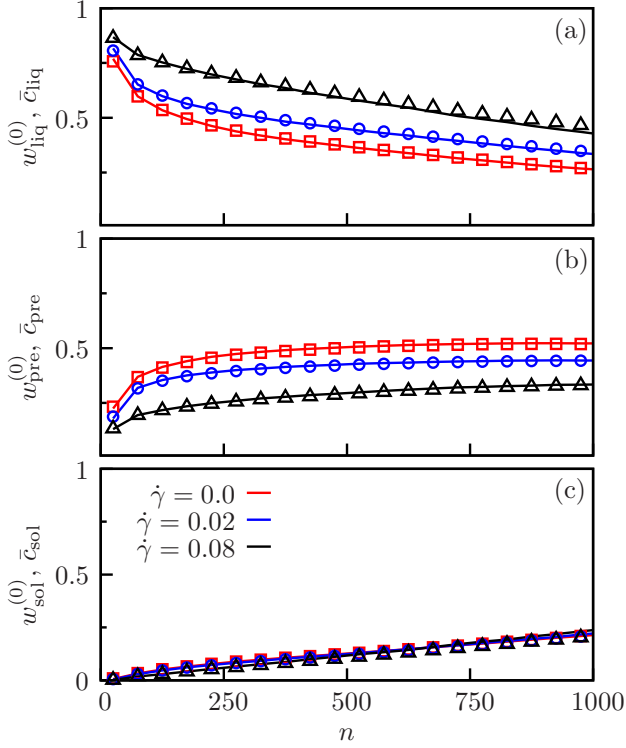


FIG. 3: (a) Liquid, (b) pre-structured, and (c) solid fraction of the quasi-stationary populations  $\mathbf{w}^{(0)}$  as function of  $n$  (lines) and the corresponding actual populations  $\bar{\mathbf{c}}$  (symbols).

average populations of local structures measured in the simulations should be equal to the stationary eigenvector:  $\bar{\mathbf{c}}(n) \approx \mathbf{w}^{(0)}(n)$ . Indeed, as shown in Fig. 3, this is the case to a very good degree. Shown are the actual and quasi-stationary fractions of particles in a liquid, pre-structured, and solid local environment, where  $\bar{c}_{\text{sol}} \equiv \bar{c}_{\text{hcp}} + \bar{c}_{\text{bcc}} + \bar{c}_{\text{fcc}}$  and  $w_{\text{sol}}^{(0)} \equiv w_{\text{hcp}}^{(0)} + w_{\text{bcc}}^{(0)} + w_{\text{fcc}}^{(0)}$  sum the contributions of all crystalline particles. Deviations are small but increase with increasing strain rate/cluster size up to maximal 7% at  $n = 1000$ . This demonstrates that the growth of the cluster is a slow process and that the lag time  $\delta t$  is sufficient to sample the fast dynamics.

### III. RESULTS

#### A. Crystallization rate

We first examine the overall effect of shear flow on the total time it takes a supersaturated suspension to crystallize. According to the protocol described above, we start with a supersaturated, fluid suspension and apply shear flow at  $t = 0$ . Once the largest cluster in the suspension has reached a size of  $n = 800$ , we stop the simulation and denote the elapsed time as  $\tau_x$ . The stopping size is clearly larger than the critical nucleus size but small enough (compared to the total number of particles) to minimize finite-size effects due to the periodic boundaries. Av-

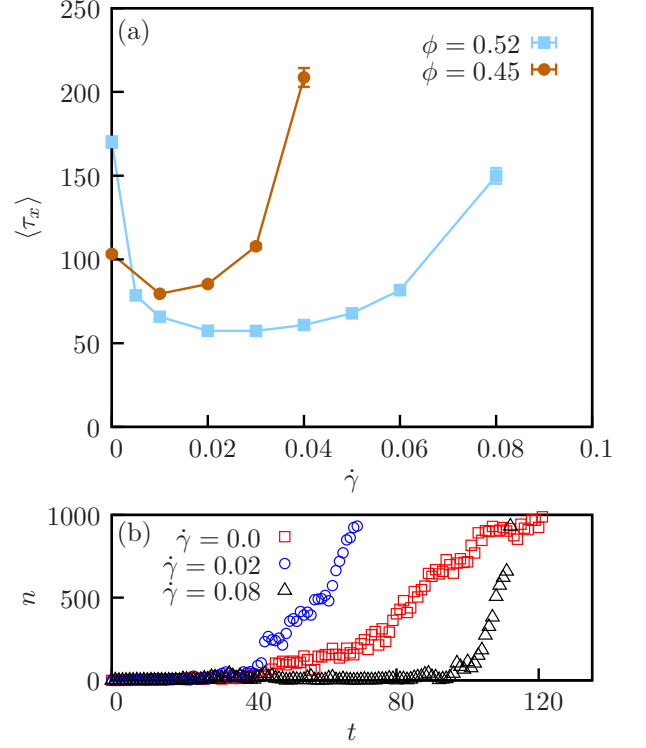


FIG. 4: (a) Average times of crystallization  $\tau_x$  as a function of the shear rate with standard error bars for the estimation of the mean value. (b) Temporal development of  $n$  for typical runs at  $\phi = 0.52$  for the strain rates  $\dot{\gamma} = 0.0, 0.02$ , and  $0.08$ .

eraging over 500 independent runs for each strain rate, we obtain a non-monotonous dependence of  $\tau_x$  on  $\dot{\gamma}$ , see Fig. 4(a). For vanishing strain rate, the denser suspension takes longer to crystallize. Increasing the strain rate,  $\tau_x$  decreases for both densities. For the larger density, however, the decrease is much stronger and  $\tau_x$  drops even below the value for the less dense system. In both cases, we observe an optimal strain rate  $\dot{\gamma}^*$  at which the crystallization process is fastest with  $\dot{\gamma}^* \simeq 0.02$  and  $\dot{\gamma}^* \simeq 0.01$  for  $\phi = 0.52$  and  $\phi = 0.45$ , respectively. At high strain rates, crystallization becomes rare. Already for  $\dot{\gamma} = 0.1$  and  $\dot{\gamma} = 0.05$ , for  $\phi = 0.52$  and  $\phi = 0.45$ , respectively, a significant part of the 500 runs did not crystallize within  $2 \times 10^6$  time steps. We thus find an accelerated crystallization for small but nonvanishing strain rates, while for higher  $\dot{\gamma}$  crystallization is more and more suppressed.

Following the development of the size  $n$  of the largest cluster in the suspension in time, we find qualitative differences in the way the crystalline state is reached for different strain rates, see Fig. 4(b). Without shear flow, the system starts crystallizing quickly but the cluster grows slowly, whereas in the high-shear case, the system stays at a low  $n$  for some time before crystallization is initiated. Afterwards, the largest cluster develops rapidly. Close to the optimal strain rate, we find features of both limiting cases. The crystallization process starts almost as early as without shear flow, but progresses more rapidly later

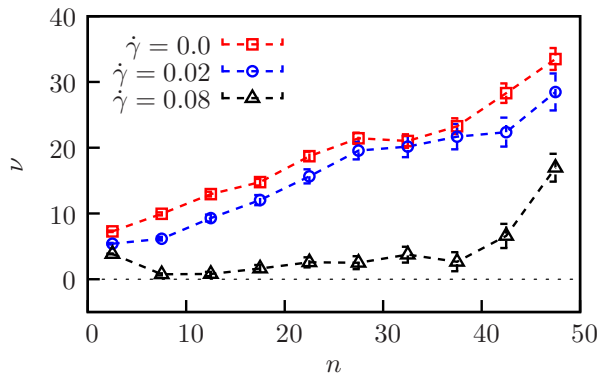


FIG. 5: Average growth rate of the size  $n$  of the largest cluster at the nucleation stage ( $n$  small) as a function of  $n$  for different strain rates at  $\phi = 0.52$ . For large  $\dot{\gamma}$ , the growth rate of the largest cluster is strongly suppressed in the interval  $10 \lesssim n \lesssim 40$ .

on.

## B. Shear flow suppresses nucleation

### 1. Growth rate

A pertinent quantity to study is the growth rate of the largest cluster

$$\nu(n) \equiv \left\langle \frac{n(t + \delta t) - n(t)}{\delta t} \delta_{n, n(t)} \right\rangle / Z_n \quad (16)$$

averaged at fixed  $n$ , i. e., at a specific stage in the development of the largest cluster. The dot denotes the rate of change. In Fig. 5, we show this quantity for  $n \leq 50$ . For  $\dot{\gamma} = 0.02$ , the average growth rate is only marginally smaller than the one in the unsheared case. For  $\dot{\gamma} = 0.08$ , however, the growth is strongly suppressed in a broad range  $10 \lesssim n \lesssim 40$ . This result could be due to a shear-induced inhibition of the formation, or due to a shear-induced destruction of small clusters. Either way, the likelihood for the formation of a critical cluster is strongly reduced. In the remainder of this subsection, we discuss the relevance of these mechanisms.

### 2. Effect on pre-structured liquid

Following the two-stage scenario for nucleation, a crystalline cluster is not likely to occur in the middle of an entirely random distribution of particles. Rather, in a region of the liquid which has already acquired a loosely ordered state, fluctuations transforming parts of this pre-structured liquid into a crystal are much more likely to occur. This scenario also holds in the system studied here: While the fraction of pre-structured particles transferring to a solid state is on the order of a few percent,  $T_{\text{pre} \rightarrow \text{sol}} \sim 0.03$ , the corresponding fraction of particles

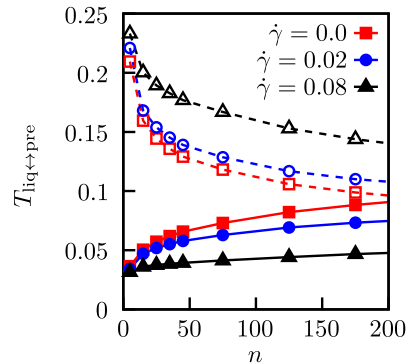


FIG. 6: Transfer matrix components for transitions from the liquid to the pre-structured state (solid lines) and the corresponding backwards transitions (dashed lines) for volume fraction  $\phi = 0.52$  as a function of cluster size  $n$ .

converting directly from liquid to solid is smaller by more than three orders of magnitude,  $T_{\text{liq} \rightarrow \text{sol}} < 10^{-5}$ .

In order to study the effect of shear flow on the structure of the liquid, we record the transfer matrix components  $T_{\text{liq} \rightarrow \text{pre}}$  and corresponding backward component  $T_{\text{pre} \rightarrow \text{liq}}$ , see Fig. 6. Note that  $T_{i \rightarrow j}$  describes the *fraction* of particles in structure  $i$  transferring on average to structure  $j$  in the following time interval  $\delta t$ . Hence, the actual net current of particles changing from  $i$  to  $j$  depends as well on the population in these states. Hence, although  $T_{\text{liq} \rightarrow \text{pre}} < T_{\text{pre} \rightarrow \text{liq}}$ , the net current of particles is still directed from liquid to pre-structured, as the liquid state contains much more particles than the pre-structured one at this early stage in the crystallization process. In Fig. 6, we show  $T_{\text{liq} \rightarrow \text{pre}}$  and  $T_{\text{pre} \rightarrow \text{liq}}$  for three different strain rates. We find that shear flow has a significant influence on the development of structure in the liquid. On the one hand, the establishment of bonds is inhibited, as can be seen from the reduced values for  $T_{\text{liq} \rightarrow \text{pre}}$ . On the other hand, structure in the liquid is destroyed, resulting in an enhanced value for  $T_{\text{pre} \rightarrow \text{liq}}$ . Consequently, compared to the unsheared case, we find a much smaller fraction of pre-structured particles  $\bar{c}_{\text{pre}}$  both in the stationary and in the actual composition of the suspension for  $\dot{\gamma} = 0.08$ , see Fig. 3(b). In other words, shear flow prevents the liquid from developing a loose structure.

In Fig. 7, we follow the evolution of the largest crystalline cluster for strain rates  $\dot{\gamma} = 0.0$  and  $0.08$ . Clearly, in both cases the crystallization process is dominated by a single cluster. Note that crystalline clusters (large spheres in blue, gray, and red) are composed of different local structures, but there seems to be no tendency for a certain structure type to form a core or surface (e.g., a core of fcc particles with a cluster-fluid interface formed by bcc particles). Crystalline clusters are surrounded by pre-structured particle (small green spheres). Although most prominent in the vicinity of solid clusters, this loose structure can be found throughout the suspension. In the strongly sheared case, however, we observe considerably less pre-structured particles than in the unsheared sus-



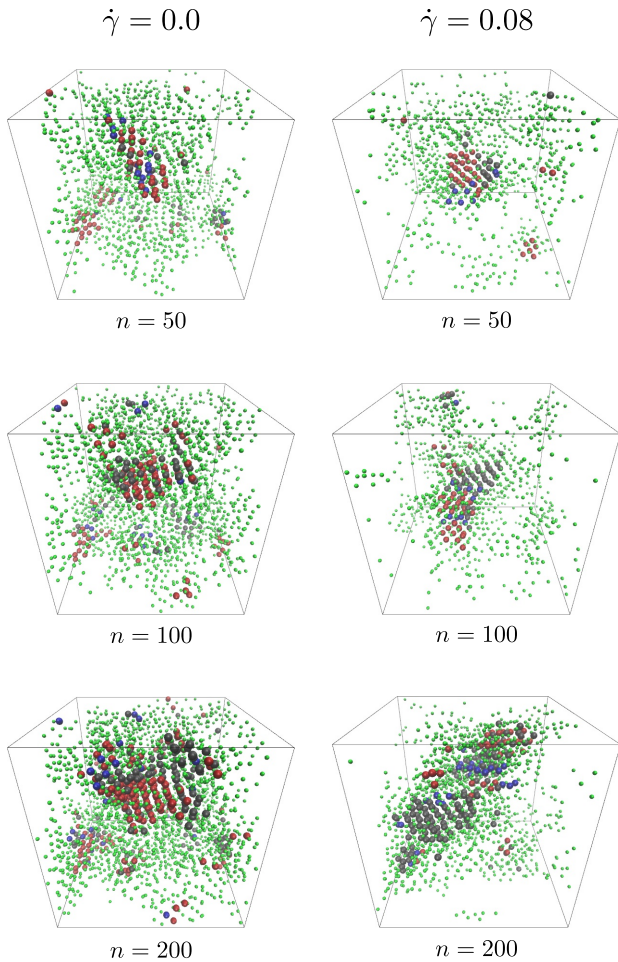


FIG. 7: Snapshots of the suspension during the crystallization process for  $\dot{\gamma} = 0.0$  (left column) and  $\dot{\gamma} = 0.08$  (right column) for three different sizes of the largest cluster  $n$ . The large spheres are solid particles with hcp (blue), bcc (gray), and fcc-structured (red) environments. Pre-structured particles are shown as small sphere (green), whereas liquid particles are not shown for clarity.

pension, which indicates the shear-induced disruption of a loosely structured fluid.

### 3. From pre-structured to solid

Once a pre-structured but still amorphous environment has formed, the pre-structured liquid has yet to transform into a crystalline cluster. Hence, the next step is to focus on the influence of shear flow on the second part of the transition from liquid to crystal. We trace the transitions between pre-structured and the crystalline structures hcp, bcc, and fcc and show the corresponding transfer components  $T_{j \rightarrow i}$  in Fig. 8. Here, the influence of the shear flow is much smaller than for the transitions between liquid and pre-structured. The rates from the crystalline states to the pre-structured one describe the destruction of crystalline clusters. Interestingly, these

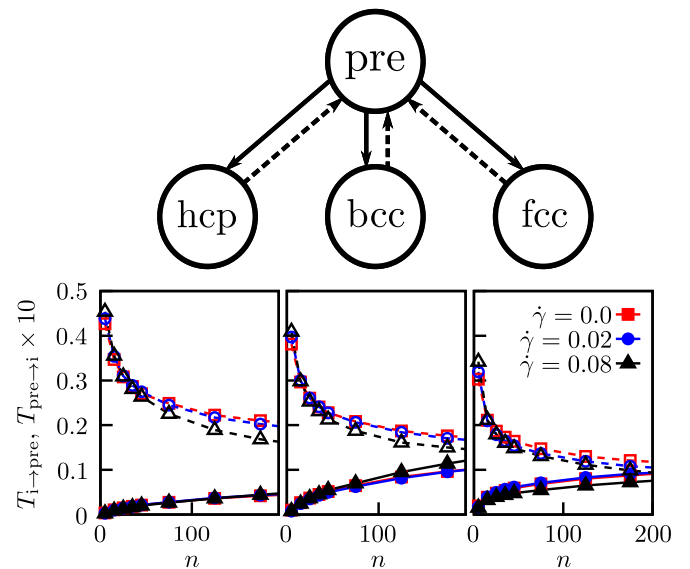


FIG. 8: Transfer matrix components for transitions from the pre-structured state to hcp, bcc, and fcc (from left to right, solid lines) scaled by a factor 10 and their corresponding backwards fluxes (dashed) for  $\dot{\gamma} = 0.0, 0.02$ , and  $0.08$ .

are not enhanced by the shear flow but even somewhat reduced. Transitions into the different crystalline states are also barely affected by the shear flow. Hence, we find that the shear flow is not strong enough to actually destroy or shrink clusters once they have formed.

## C. Shear flow enhances growth of clusters

### 1. Growth rate

Complementary to Fig. 5, we now plot the growth rate Eq. (16) over a wider range of cluster sizes shown in Fig. 9. Note that for the larger clusters considered here, we need to increase the time interval over which the change in  $n$  is evaluated to  $\delta t = 5000\Delta t$  in order to separate the growth trend from the fluctuations. Compared to the unsheared case, the growth rate is enhanced significantly once the shear flow is switched on. Furthermore, for cluster sizes  $n \gtrsim 400$  the growth rate is dominated by a linear term, the slopes of which themselves grow proportional with the strain rate, see inset in Fig. 9. We observe the same behavior for  $\phi = 0.45$  (data not shown). The dominant contribution of the shear flow to the growth rate for  $n \gtrsim 400$  is thus a linear term of the form

$$\nu(n) = B\dot{\gamma}n, \quad (17)$$

where the proportionality constants for the slopes  $B$  can be determined from least-square fits to the data. We find  $B = 2.28 \pm 0.10$  and  $2.75 \pm 0.16$  for  $\phi = 0.52$  and  $\phi = 0.45$ , respectively. This strongly shear-dependent growth rate reflects the enhanced cluster growth for large

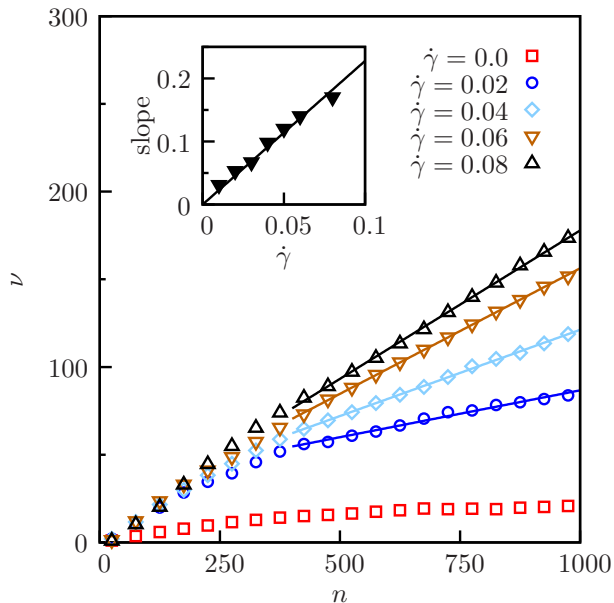


FIG. 9: Average growth rate of the largest cluster as a function of  $n$  for different strain rates for volume fraction  $\phi = 0.52$ . The solid lines are linear fits to the data for  $n \geq 400$ . Inset: Slope of the fit functions as a function of strain rate  $\dot{\gamma}$ . The solid line is a linear fit starting at the origin.

times as shown in Fig. 4(b) on a more systematic level. We now discuss two possible mechanisms of how shear flow influences the growth stage of crystallization.

### 2. Mechanism I: Convection

A growth rate that is a linear function of  $n$  might arise from convection, which can be understood as follows. We assume that particles in the vicinity of a crystalline nucleus are more likely to crystallize. Shear flow enhances the number of particles passing through this direct vicinity of the nucleus which we model as a sphere with radius  $R$ . The particle current entering this sphere caused by the shear flow reads

$$\frac{1}{2} \int_{\mathcal{S}} \rho_l \dot{\gamma} |y \mathbf{e}_x \cdot d\mathbf{S}| = \frac{4}{3} \rho_l R^3 \dot{\gamma} \propto \dot{\gamma} n \quad (18)$$

with the surface of the sphere  $\mathcal{S}$  and the number density of particles in the liquid  $\rho_l \equiv \pi\phi/6$ . The particle current is thus proportional to the size of the cluster, and proportional to the strain rate  $\dot{\gamma}$ . Hence, we obtain the functional form of Eq. (17) where the free parameter  $B$  takes into account deviations from the spherical shapes of the cluster and the probability with which particles become solid (attach to the cluster).

### 3. Mechanism II: bcc grows fastest

A second explanation for an enhanced growth rate might be that one of the local structures can be grown faster. In Fig. 10(a)-(c), we show the components of the transfer matrix for transitions between the three solid structures. The most prominent effect of the shear flow is that the largest strain rate strongly facilitates transitions towards the bcc structure. For the other transitions, the effect of the shear flow is weaker. The rates towards the hcp structure grow slightly with increasing  $\dot{\gamma}$  and the optimal strain rate  $\dot{\gamma} = 0.02$  enhances transitions from bcc to fcc.

Fig. 10(d) shows the relative composition of all solid particles in the suspension as a function of cluster size  $n$ . For small  $\dot{\gamma}$ , most solid particles belong to fcc, which is the stable equilibrium structure. Interestingly, even in the unsheared case does the fraction of fcc particles slightly decrease as the cluster becomes bigger. In consistency with the shear dependence of the transition rates, at the optimal strain rate  $\dot{\gamma} = 0.02$ , the fraction of bcc particles is decreased and the number of fcc particles is increased, whereas the shear flow has almost no influence of the fraction of hcp particles. Quite in contrast, the bcc particles overtake the fcc particles at the higher strain rate  $\dot{\gamma} = 0.08$  and become the dominant structural type. As can be seen in the snapshots in Fig. 7, shear flow allows for much larger bcc domains. This can be interpreted as a consequence of the Ostwald step rule: in the unsheared case bcc is more easily formed but fcc is the more stable structure. Shear flow stabilizes bcc in relation to fcc and hcp, thus allowing for larger fractions of this structure type. If bcc is indeed the fastest growing structure, this mechanism would also lead to an enhanced crystalline growth.

## IV. CONCLUSIONS

We have performed Langevin dynamics simulations to investigate the overall effect of weak linear shear flow on the crystallization process in a model colloidal suspension. We found that the time it takes for the suspension to become solid exhibits a minimum at a finite strain rate. This can be explained as the result of two counteracting effects: at the early nucleation stage, the shear flow inhibits the formation of a critical nucleus, while at the later stage growth is enhanced. Both effects become manifest in the growth rate of the largest cluster, see Fig. 5 and Fig. 9. For larger strain rates the growth rate of small clusters is vanishingly small, whereas already small strain rates significantly speed up the growth process of the crystalline clusters after nucleation.

To gain further insight into the different mechanism, we have employed a discrete state model. The state space of this discrete model comprises the relevant local structural environments of a *single* particle. The microscopic environment of a particle might be fluid or solid. We



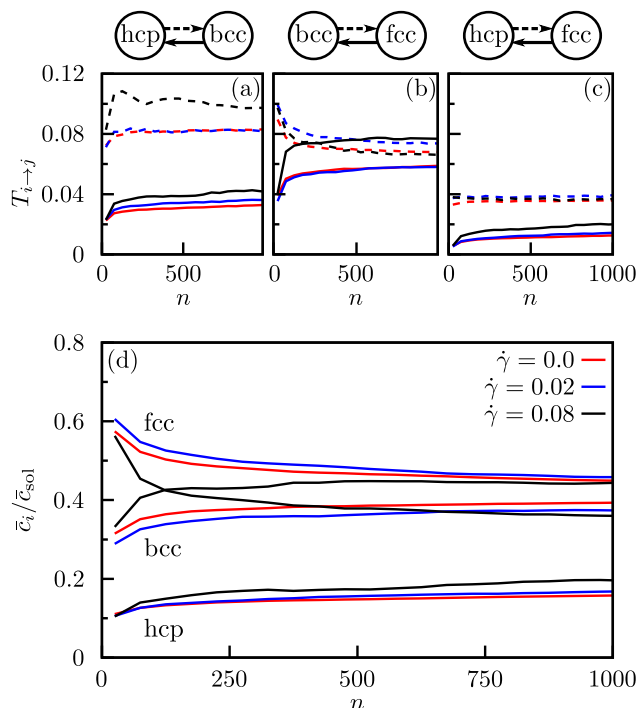


FIG. 10: Transfer matrix components for the transitions between the three solid local structures: (a) hcp and bcc, (b) bcc and fcc, and (c) hcp and fcc. (d) Relative populations of solid particles in structure hcp, bcc, and fcc  $\bar{c}_i / \bar{c}_{\text{sol}}$  measured in the simulations.

further distinguish between the unordered liquid and a pre-structured liquid, which still is amorphous but where already a loose structure between neighbors has formed as determined from a bond criterion. The solid particles are classified according to their crystal structure as either fcc, bcc, or hcp; leading to a total of five discrete states. From the simulation data we can measure the populations, i.e., the fraction of particles that resides in each structure. Since the simulations advance from the initial liquid towards the full crystal, these populations change over time. We have found it convenient to calculate conditional averages with respect to the size of the largest cluster. Moreover, we have determined the fluxes between the discrete states, from which we built a transfer matrix. The quasi-stationary state of this transfer matrix

agrees well with the measured actual populations.

Nucleation in our model system clearly proceeds from liquid through pre-structured to one of the crystalline structures. The effect of shear flow is to disrupt the formation of the pre-structured regions, see Fig. 6. Consequently, there are fewer pre-structured particles and the probability to form a critical nucleus is drastically lowered. On the other hand, once a critical droplet of solid particles has formed, the growth rate is enhanced by the shear flow. The emerging functional form (17) can be explained by convection alone: The flow field constantly changes the vicinity of crystalline clusters and is thus able to enhance the number of liquid particles under the “influence” of a crystalline cluster. However, the shear flow also influences the composition of the cluster, hinting at a second mechanism. We found that shear flow facilitates transitions towards the bcc structure and thus enhances the fraction of bcc particles in the cluster. The stable bulk structure is fcc and, therefore, there is a driving force towards fcc. Destabilizing fcc (or stabilizing bcc) allows for larger domains of bcc particles without the need to convert bcc, which in turn allows the cluster to grow faster.

Our data show that the depth of the minimum in the duration for the crystallization process is much smaller for a lower supersaturation. This point entails the question whether there is a lower bound on the density below which this minimum vanishes. How the existence and depth of this minimum depends on the supersaturation remains a topic for future investigation. Moreover, it would be interesting to study the influence of hydrodynamic interactions on the crystallization process [52] under shear in general, and on the magnitude and the existence of such an optimal strain rate in particular. Beyond the insights we could gain for our specific model, we believe that the combination of techniques presented here will prove useful in the study of nucleation and related processes.

## Acknowledgments

We acknowledge financial support by Deutsche Forschungsgemeinschaft (Grant No. SE-1119/3).

- 
- [1] H. Löwen, Phys. Rep. **237**, 249 (1994).
  - [2] R. Becker and W. Döring, Annalen der Physik **416**, 719 (1935).
  - [3] J. Frenkel, *Kinetic theory of liquids* (Clarendon Pr., Oxford, 1947).
  - [4] S. P. Das, *Statistical Physics of Liquids at Freezing and Beyond* (Cambridge Univ. Press, 2011).
  - [5] A. Onuki, J. Phys.: Condens. Matter **9**, 6119 (1997).
  - [6] J. Vermant and M. J. Solomon, J. Phys.: Condens. Matter **17**, R187 (2005).
  - [7] S. Butler and P. Harrowell, Nature **415**, 1008 (2002).
  - [8] S. Butler and P. Harrowell, J. Chem. Phys. **118**, 4115 (2003).
  - [9] B. J. Ackerson and P. N. Pusey, Phys. Rev. Lett. **61**, 1033 (1988).
  - [10] Y. D. Yan, J. K. G. Dhont, C. Smits, and H. N. W. Lekkerkerker, Physica A **202**, 68 (1994).
  - [11] M. D. Haw, W. C. K. Poon, and P. N. Pusey, Phys. Rev. E **57**, 6859 (1998).
  - [12] R. M. Amos, J. G. Rarity, P. R. Tapster, T. J. Shepherd,

- and S. C. Kitson, Phys. Rev. E **61**, 2929 (2000).
- [13] P. Panine, T. Naranyan, J. Vermant, and J. Mewis, Phys. Rev. E **66**, 022401 (2002).
  - [14] A. V. Mokshin and J.-L. Barrat, Phys. Rev. E **77**, 021505 (2008).
  - [15] A. Nikoubashman, G. Kahl, and C. N. Likos, Phys. Rev. Lett. **107**, 068302 (2011).
  - [16] T. Palberg, W. Mönch, J. Schwarz, and P. Leiderer, J. Chem. Phys. **102**, 5082 (1995).
  - [17] S. Butler and P. Harrowell, Phys. Rev. E **52**, 6 (1995).
  - [18] R. Blaak, S. Auer, D. Frenkel, and H. Löwen, Phys. Rev. Lett. **93** (2004).
  - [19] P. Holmqvist, M. P. Lettinga, J. Buitenhuis, and J. K. G. Dhont, Langmuir **21**, 10976 (2005).
  - [20] Y. L. Wu, D. Derks, A. van Blaaderen, and A. Imhof, Proc. Natl. Acad. Sci. U.S.A. **106**, 10564 (2009).
  - [21] A. Penkova, W. Pan, F. Hodjaoglu, and P. G. Vekilov, Ann. N. Y. Acad. Sci. **1077**, 214 (2006).
  - [22] J. J. Cerdà, T. Sintès, C. Holm, C. M. Sorensen, and A. Chakrabarti, Phys. Rev. E **78**, 031403 (2008).
  - [23] R. J. Allen, C. Valeriani, S. Tanase-Nicola, P. R. ten Wolde, and D. Frenkel, J. Chem. Phys. **129**, 134704 (2008).
  - [24] A. V. Mokshin and J.-L. Barrat, Phys. Rev. E **82**, 021505 (2010).
  - [25] K. Schätzel and B. J. Ackerson, Phys. Rev. E **48**, 3766 (1993).
  - [26] J. L. Harland and W. van Megen, Phys. Rev. E **55**, 3054 (1997).
  - [27] C. Sinn, A. Heymann, A. Stipp, and T. Palberg, Prog. Colloid Polym. Sci. **118**, 266 (2001).
  - [28] U. Gasser, E. R. Weeks, A. Schofield, P. N. Pusey, and D. A. Weitz, Science **292**, 258 (2001).
  - [29] U. Gasser, J. Phys.: Condens. Matter **21**, 203101 (2009).
  - [30] A. Yethiraj and A. van Blaaderen, Nature **421**, 513 (2003).
  - [31] C. Dellago, P. G. Bolhuis, and P. L. Geissler, Adv. Chem. Phys. **123**, 1 (2002).
  - [32] A. C. Pan and D. Chandler, J. Phys. Chem. B **108**, 19681 (2004).
  - [33] R. J. Allen, P. B. Warren, and P. R. ten Wolde, Phys. Rev. Lett. **94**, 018104 (2005).
  - [34] R. J. Allen, C. Valeriani, and P. R. ten Wolde, J. Phys.: Condens. Matter **21**, 463102 (2009).
  - [35] G. M. Torrie and J. P. Valleau, J. Comput. Phys. **23**, 187 (1977).
  - [36] D. Frenkel and B. Smit, *Understanding Molecular Simulation: From Algorithms to Applications* (Academic Press, San Diego, 2002).
  - [37] S. R. Rastogi, N. J. Wagner, and S. R. Lustig, J. Chem. Phys. **104**, 9234 (1996).
  - [38] J. F. Lutsko and G. Nicolis, Phys. Rev. Lett. **96**, 046102 (2006).
  - [39] T. Schilling, H. J. Schöpe, M. Oettel, G. Opletal, and I. Snook, Phys. Rev. Lett. **105**, 025701 (2010).
  - [40] W. Lechner, C. Dellago, and P. G. Bolhuis, Phys. Rev. Lett. **106**, 085701 (2011).
  - [41] J. Russo and H. Tanaka, Sci. Rep. **2** (2012).
  - [42] M. P. Allen and D. J. Tildesley, *Computer Simulation of Liquids* (Clarendon Press, Oxford, 1987).
  - [43] M. O. Robbins, K. Kremer, and G. S. Grest, J. Chem. Phys. **88**, 3286 (1988).
  - [44] E. J. Meijer and D. Frenkel, J. Chem. Phys. **94**, 2269 (1991).
  - [45] L. V. Woodcock, Nature **385**, 141 (1997).
  - [46] J. Zhu, M. Li, R. Rogers, W. Meyer, R. H. Ottewill, S.-S. Crew, W. B. Russel, and P. M. Chaikin, Nature **387**, 883 (1997).
  - [47] W. Ostwald, Z. Phys. Chem. **22**, 289 (1897).
  - [48] P. R. ten Wolde and D. Frenkel, Phys. Chem. Chem. Phys. **1**, 2191 (1999).
  - [49] P. J. Steinhardt, D. R. Nelson, and M. Ronchetti, Phys. Rev. B **28**, 2 (1983).
  - [50] W. Lechner and C. Dellago, J. Chem. Phys. **129**, 114707 (2008).
  - [51] P. R. ten Wolde and M. J. Ruiz-Montero, J. Chem. Phys. **104**, 9932 (1996).
  - [52] M. Radu and T. Schilling, arXiv:1301.5592 (2013).